ACS Energy LETTERS

Cite This: ACS Energy Lett. 2018, 3, 1443−1449

A One-Dimensional Organic Lead Chloride Hybrid with Excitation-Dependent Broadband Emissions

Guanhong Wu,[†,⊥] Chenkun Zhou,[‡,⊥] Wenmei Ming,[§] Dan Han,[§,∥,#] Shiyou Chen,[#] Dong Yang,[◆] Tiglet Besara,[¶] Jennifer Neu,[¶] Theo Siegrist,[¶] Mao-Hua Du,[*,§] Biwu Ma,[*,‡,∇,○] and Angang Dong[*,†]

[†] iChem, Shanghai Key Laboratory of Molecular Catalysis and Innovative Materials, and Department of Chemistry, Fudan University, Shanghai 200433, China

[‡] Department of Chemical and Biomedical Engineering, FAMU-FSU College of Engineering, Tallahassee, Florida 32310, United States

[§] Materials Science and Technology Division, Oak Ridge National Laboratory, Oak Ridge, Tennessee 37831, United States

[∥] Key Laboratory of Polar Materials and Devices (Ministry of Education), East China Normal University, Shanghai 200241, China

[#] Department of Physics, East China Normal University, Shanghai 200241, China

[∇] Materials Science and Engineering Program, Florida State University, Tallahassee, Florida 32306, United States

[○] Department of Chemistry and Biochemistry, Florida State University, Tallahassee, Florida 32306, United States

[◆] State Key Laboratory of Molecular Engineering of Polymers and Department of Macromolecular Science, Fudan University, Shanghai 200433, China

[¶] National High Magnetic Field Laboratory, Florida State University, Tallahassee, Florida 32310, United States

Supporting Information

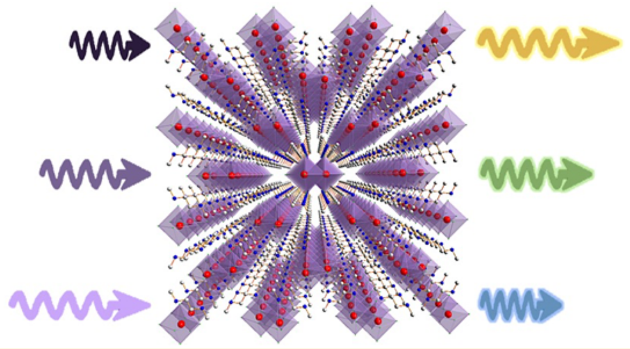

ABSTRACT: Organic−inorganic metal halide hybrids have emerged as a new class of materials with fascinating optical and electronic properties. The exceptional structure tunability has enabled the development of materials with various dimensionalities at the molecular level, from three-dimensional (3D) to 2D, 1D, and 0D. Here, we report a new 1D lead chloride hybrid, $C_4N_2H_{14}PbCl_4$, which exhibits unusual inverse excitation-dependent broadband emission from bluish-green to yellow. Density functional theory calculations were performed to better understand the mechanism of this excitation-dependent broadband emission. This 1D hybrid material is found to have two emission centers, corresponding to the self-trapped excitons (STEs) and vacancy-bound excitons. The excitation-dependent emission is due to different populations of these two types of excitons generated at different excitation wavelengths. This work shows the rich chemistry and physics of organic−inorganic metal halide hybrids and paves the way to achieving novel light emitters with excitation-dependent broadband emissions at room temperature.

Excitation-dependent photoluminescence (PL) refers to a unique photophysical property that photoluminescence emission wavelength can be tuned simply by manipulating the excitation wavelength, without changing the size or chemical composition of a material. A universal mechanism to generally interpret this phenomenon is still lacking, but it is believed that several effects, including the quantum confinement effect, surface traps, and edge states, might jointly lead to the excitation-dependent emission.[1] In practice, excitation-dependent emission, which mainly exists in quantum dot (QD) systems, such as carbon nanodots,[2−4] graphene quantum dots,[5−12] and MoS_2 quantum dots,[13] was normally identified as a positive correlation between excitation and emission wavelength. In addition, such a phenomenon was also observed

Received: April 25, 2018
Accepted: May 23, 2018
Published: May 23, 2018

DOI: 10.1021/acsenergylett.8b00661
ACS Energy Lett. 2018, 3, 1443−1449

in $(C_4N_2H_{14}Br)_4SnBr_3I_3$ mixed-halide hybrid at 77 K, which is attributed to a combination of decays from different excitation-dependent distorted structures.[14] Nevertheless, a deep and sophisticated insight into the mechanism for the excitation-dependent PL is highly instructive for modulating the luminescence, which would be quite beneficial for their applications.

Low-dimensional organic−inorganic metal halide hybrids, known as the derivatives of the conventional ABX_3 perovskite structure,[15−17] have emerged as a new class of functional materials with remarkable optical and electronic properties significantly different from those of their 3D counterparts.[18,19] For instance, low-dimensional metal halide hybrids, such as corrugated 2D[20−22] and 1D hybrids,[23−26] exhibit strong structural distortion associated with significant quantum confinement effects, leading to the formation of both free exciton (FE) and self-trapped exciton (STE) excited states upon photoexcitation. As a result, broadband emission with large Stokes shift can be achieved, providing access to single-component white light emitters. In addition, the photophysics of low-dimensional metal halide hybrids has been shown to be highly tunable by engineering the chemical composition and dimensionality.[17] While low-dimensional metal halide hybrids have aroused tremendous interest during the past few years, the research in this area is still in the early stage, significantly behind the efforts in the well-known 3D perovskites. To date, only very few 1D organic metal halide hybrids have been developed and investigated.[23−28]

Herein, we report the synthesis, characterization, and computational studies on a 1D organic lead chloride hybrid single crystal, $C_4N_2H_{14}PbCl_4$, a sibling of previously reported 1D $C_4N_2H_{14}PbBr_4$ and $C_4N_2H_{14}SnBr_4$.[24,26] Interestingly, this new 1D organic metal halide hybrid exhibits photophysical properties that are significantly different from those two, with inverse excitation-dependent broadband emission between bluish-green and yellow. These emissions exhibit ultralarge Stokes shift from 1.40 to 1.70 eV, with photoluminescence quantum efficiencies (PLQEs) from 6% to 18%. Through theoretical and experimental verifications, we attribute this phenomenon to the competition of STEs and vacancy-bound excitons.

The $C_4N_2H_{14}PbCl_4$ single crystals were prepared by antisolvent vapor-assisted crystallization. Briefly, combining lead(II) chloride with *N,N′*-dimethylethylene-1,2-diammonium chloride salts in dimethyl sulfoxide (DMSO) at room temperature leads to the nucleation of $C_4N_2H_{14}PbCl_4$. Crystals were obtained after diffusing acetone into the DMSO solution for a few days. The structure of $C_4N_2H_{14}PbCl_4$ is shown in Figure 1a−c, and its detailed structural information is summarized in Tables S1, S2, and S3. Similar to previous reports,[24,26] this 1D organic metal halide hybrid can be considered as the assembly of core−shell quantum wires that consist of $[PbCl_4]^{2-}$ double chains coated with $C_4N_2H_{14}^{2+}$ cations. The inorganic frameworks are made of double edge-sharing octahedral $PbCl_6^{4-}$ units, as shown in Figure 1c. Despite these similarities, their structures are distinct, especially when speaking of the degree of distortion of the octahedron, which can be quantified by several parameters, including halide distance deviation (DI(X−X)), bond-length distortion (Δ_{oct}), octahedral elongation (λ_{oct}), octahedral angle variance (σ_{oct}^2), and volume discrepancy (V).[29] Table 1 shows the comparison of octahedral distortion between 1D $C_4N_2H_{14}PbBr_4$, $C_4N_2H_{14}SnBr_4$, and $C_4N_2H_{14}PbCl_4$. It is clear that the degree of distortion follows the trend $C_4N_2H_{14}SnBr_4 > C_4N_2H_{14}PbCl_4 > C_4N_2H_{14}PbBr_4$, from which we might expect some totally different photophysical properties. The powder X-ray diffraction (PXRD) pattern of the ball-milled powders of the single crystals shows almost identical features with that of the simulated PXRD pattern (Figure 1d).

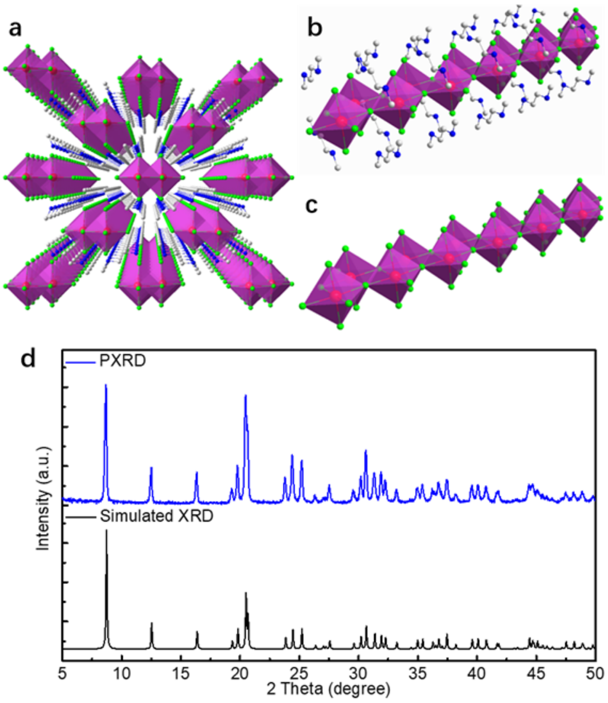

Figure 1. Structural characterization of 1D $C_4N_2H_{14}PbCl_4$ single crystal. (a) Structure of $C_4N_2H_{14}PbCl_4$ (red spheres, lead atoms; green spheres, chloride atoms; blue spheres, nitrogen atoms; gray spheres, carbon atoms; purple polyhedrons, $PbCl_6^{4-}$ octahedrons; hydrogen atoms were hidden for clarity). (b) View of a single lead chloride quantum wire wrapped by organic cations. (c) View of a single lead chloride quantum wire with edge-sharing octahedrons. (d) Powder X-ray diffraction (PXRD) pattern of 1D $C_4N_2PbCl_4$ crystals. The simulated PXRD pattern is also provided for comparison.

Table 1. Comparison of Distortions of "PbX_6" Octahedra for Various 1D Organic Metal Halide Hybrids

	$C_4N_2H_{14}PbBr_4$	$C_4N_2H_{14}SnBr_4$	$C_4N_2H_{14}PbCl_4$
$\Delta_{oct} \times 10^4$	14.8	92.8	15.3
DI(X−X)	0.008	0.064	0.012
λ_{oct}	1.000	1.014	1.005
σ_{oct}^2	7.93	19.24	8.28
V (%)	0.040	1.500	0.003

The photophysical properties of the 1D organic lead chloride hybrid crystals were first investigated at room temperature. It is interesting that the crystals emit bluish-green and yellow light under 365 and 302 nm irradiation, respectively (Figure 2a, b). Fluorescence micrographs are shown in Figure S1. Figure 2c shows that the absorption spectrum exhibits a sharp peak around 320 nm with a long tail reaching 500 nm, suggesting the existence of multiple excited states.[30−32] The corresponding Tauc plot was calculated based on the assumptions of direct and indirect transitions (Figure S2).[33] The Tauc plot yields a direct band gap value of 3.58 eV and an indirect band gap value of 3.31 eV. The emission spectra excited by 365 and 302 nm

DOI: 10.1021/acsenergylett.8b00661
ACS Energy Lett. 2018, 3, 1443−1449

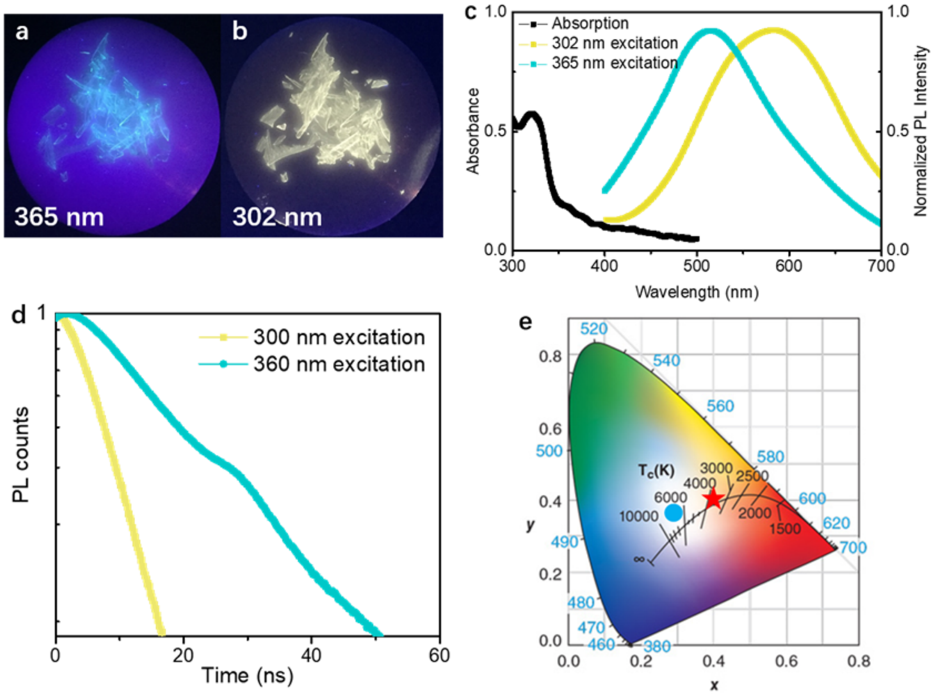

Figure 2. Photophysical properties of $C_4N_2H_{14}PbCl_4$ at room temperature. Photographs of $C_4N_2H_{14}PbCl_4$ crystals under (a) 365 nm and (b) 302 nm excitation. (c) Absorption (black) and emission spectra excited at 365 nm (green) and 302 nm (yellow), respectively. (d) Time-resolved PL decay curves of emissions excited at 300 nm (yellow trace) and 360 nm (green trace) at room temperature. (e) CIE chromaticity coordinates of emissions excited by 302 nm (red star) and 365 nm (blue circle) radiation.

both show low-energy broadband emission, featuring large Stokes shift of 1.40 eV (180 nm) and 1.68 eV (244 nm) as well as full width at half-maximum (fwhm) of 0.854 eV (179 nm) and 0.664 eV (175 nm), respectively. The high-energy band emission spectra are shown in Figure S3. The bluish-green light emission showed almost no shoulder peak, while the yellow light emission exhibited a small sharp peak around 345 nm (Figure S3b), close to the calculated direct band gap, indicating that the yellow light emission originated from direct transition associated with energy transfer/relaxation to another excited state. Figure 2d shows the PL decay curves at room temperature for both 360 and 300 nm excited emissions. The decay curves were fitted using monoexponential functions with lifetimes of 20 and 8 ns, respectively. The Commission Internationale de l'Eclairage (CIE) chromaticity coordinates were determined to be (0.29, 0.39) and (0.40, 0.43) for emissions excited by 365 and 302 nm (Figure 2e), respectively, with the corresponding correlated color temperatures of 7228 and 3880 K. The PLQEs of bluish-green and yellow light were measured to be 6% and 18%, respectively (Figure S4). Both emissions show moderate photostability in the air with a slow decrease of emission intensity under continuous Xe lamp irradiation (Figure S5). Major photophysical properties are summarized in Table 2.

To reveal the intrinsic nature of these emissions, we have measured the dependence of emission intensity on the excitation power density at room temperature. For permanent defects, concentration and lifetime of impurities are finite, which means their PL intensity would be saturated at high excitation power density.[34] As shown in Figure 3a, the intensity of the bluish-green light emission excited at 360 nm showed a linear dependence on the excitation power density up to 4 MW/cm^2, while the intensity of yellow light emission excited at 300 nm saturated at high excitation power density, suggesting that the bluish-green light emission originated from STEs, whereas the yellow light emission came from a defect-related excited state.

Table 2. Photophysical Properties of 1D $C_4N_2H_{14}PbCl_4$ Single Crystals

	λ_{ex} = 320 nm	λ_{ex} = 365 nm
λ_{abs} (nm)	320	320
λ_{em} (nm)	564	500
Stokes shift (nm) (eV)	244 (1.68)	185 (1.40)
fwhm (nm) (eV)	175 (0.664)	179 (0.854)
	124 (0.476)[a]	150 (0.725)[a]
Φ (%)	18	6
τ (ns)	8	20
	7157[a]	887[a]

[a] These data were measured at 77 K.

Interestingly, the 1D organic lead chloride hybrid crystals exhibited inverse excitation-dependent emission at both room temperature and 77 K (Figure 3b,c). Specifically, the emission peak was negatively correlated to the excitation wavelength, different from the cases in QD systems.[1] Corresponding excitation-dependent CIE chromaticity coordinates are shown in Figure S6. The lifetimes measured at 77 K were also dependent on the excitation energy, as shown in Figure 3d. In addition, PL decay curves measured at different emission wavelength were identical (Figure S7), indicating the pure origin of these emissions. The excitation spectra measured at both room temperature and 77 K exhibited a sharp peak around the band edge, with a long tail involving several peaks even more intense than the band-edge peak (Figure S8). These low-energy excitation peaks confirm the existence of subgap states again. For the temperature-dependent emission, both the above- and subgap emission showed enhanced luminescence at

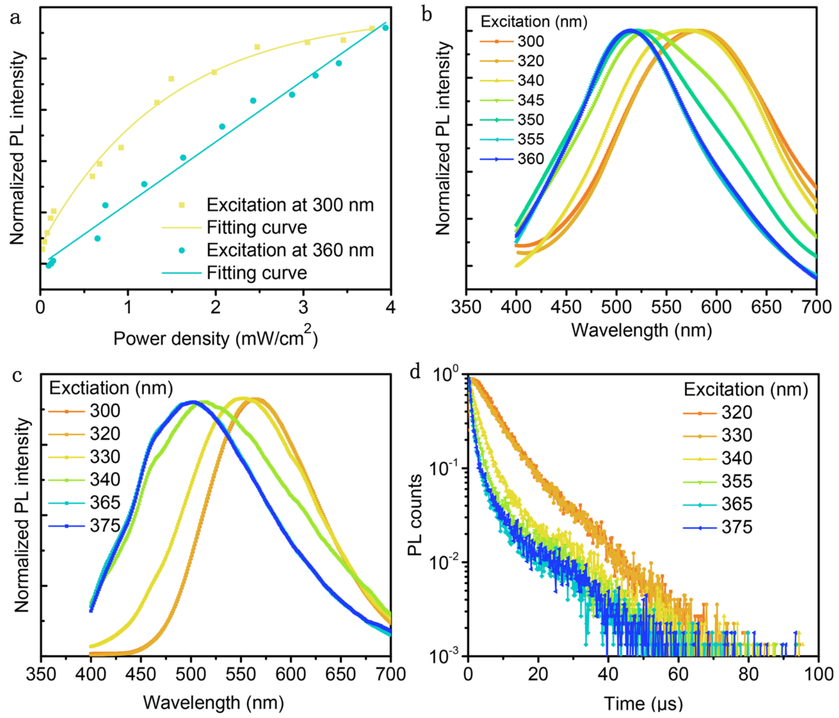

Figure 3. PL properties of $C_4N_2H_{14}PbCl_4$. (a) Plots of PL intensity as a function of excitation power density at room temperature. Normalized excitation-dependent emission spectra measured at room temperature (b) and 77 K (c). (d) Excitation-dependent PL decay curves at 77 K.

low temperature, with a slight broadening and no shift of maximum as compared to that of room temperature (Figure S9). Therefore, unlike $C_4N_2H_{14}PbBr_4$,[24] there is no equilibrium between the FE state and other excited states in $C_4N_2H_{14}PbCl_4$.

To get a deeper insight into the photophysics of this 1D organic lead chloride hybrid, we have performed density functional theory (DFT) calculations of electronic structure as well as exciton and defect properties. Figure 4 shows the band structure and the density of states calculated using PBE functionals including the spin−orbit coupling (SOC). The results show that the valence (conduction) band is made up of the antibonding states of Cl 3p and Pb 6s (Pb 6p). The electronic bands are dispersive along the Pb−Cl chain direction (k_x) but are nearly flat in directions perpendicular to the chain, consistent with the 1D structure of $C_4N_2H_{14}PbCl_4$. The band gap is indirect. The valence band maximum (VBM) is located at the T point, while the conduction band minimum (CBM) is very close to the R point along the Γ−R line.

The exciton and defect properties were calculated using hybrid PBE0 functionals including the SOC. The PBE0-optimized ground-state structure of $C_4N_2H_{14}PbCl_4$ agrees very well with the experimental results. The discrepancies between calculated and measured Pb−Cl bond lengths are all below 1.4%. The excitation of an exciton in $C_4N_2H_{14}PbCl_4$ involves the promotion of an electron from the Pb 6s orbital to the Pb 6p orbital at a 6-fold-coordinated Pb^{2+} ion. The excitation energy calculated by the PBE0 method is 4.05 eV, within the excitation band observed in experiment (Figure S8). The excited-state relaxation in Pb^{2+}-based halide hybrids typically leads to the distortion of the six Pb−halogen bonds: the contraction of the four planar Pb−halogen bonds and the elongation of the two vertical Pb−halogen bonds. We indeed stabilized such an exciton in $C_4N_2H_{14}PbCl_4$ with the two elongated vertical bonds along the 1D atomic chain direction, which induces compressive strain along the chain. However, further calculations show that the separation of the hole and the electron at the two nearest-neighbor Pb ions as shown in Figure 5 lowers the total energy by 0.26 eV. For the STE shown in Figure 5, the hole center Pb(2) attracts the adjacent Cl ions, applying tensile strain along the 1D chain, whereas the electron center Pb(1) repels the adjacent Cl ions, inducing compressive strain. The resulting strain compensation is likely the cause of the separation of the electron and the hole in the exciton. The calculated emission energy of the STE is 2.13 eV, in good agreement with the experimentally measured peak exciton emission energy of 2.48 eV (500 nm).

To explain the defect-related emission observed in experiments, we further calculated vacancy-bound excitons, because vacancies are usually the most abundant native defects in halides. The STEs can diffuse along the 1D chain and may be trapped by vacancies of Cl, Pb, and the molecular cation (V_{Cl}, V_{Pb}, V_{Mol}), leading to bound exciton emission. The calculated exciton trapping energies at V_{Cl}^{+}, V_{Mol}^{-}, and V_{Pb}^{2-} are 0.72, 0.17, and 0.15 eV, respectively (Table 3). The Cl ions are bonded to either one or three Pb ions. Among all the Cl sites, the Cl vacancy on the site of the one-fold-coordinated Cl(1) in Figure 5 is found to be the most stable. Among the three vacancies, V_{Cl} has the strongest perturbation to the exciton because the Cl(1) ion, which is directly bonded to the electron-trapping Pb(1) ion, is removed, causing strong relaxation of the exciton structure. On the other hand, V_{Pb} and V_{Mol} are the second-nearest neighbors to Pb(1) or Pb(2) in Figure 5 and thus have weak perturbation to the exciton. As a result, the emission of the V_{Cl}-bound exciton has much stronger red shifts from the STE emission than those for V_{Mol}^{-}- and V_{Pb}^{2-}-bound excitons. The calculated emission energies by the V_{Cl}^{+}-, V_{Mol}^{-}-, and V_{Pb}^{2-}-bound excitons are 1.32, 1.88, and 1.79 eV, respectively, which are red-shifted from the calculated STE emission energy (2.13 eV) by 0.81, 0.25, and 0.34 eV (Table 3). The experimentally observed defect-related emission (which is red-shifted from the

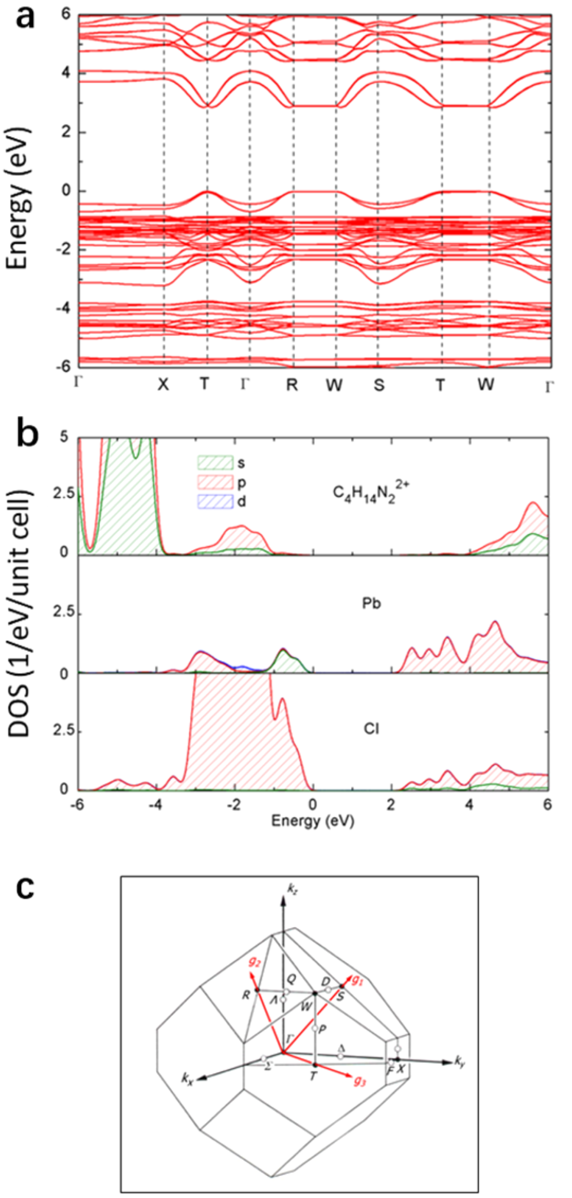

Figure 4. (a) Band structure and (b) density of states of $C_4N_2H_{14}PbCl_4$ calculated using PBE functionals. (c) The high-symmetry k points in the Brillouin zone that are included in the band structure. The g_1, g_2, and g_3 vectors are reciprocal k vectors. The PBE band gap is 2.81 eV, which is underestimated because of the well-known PBE band gap error.

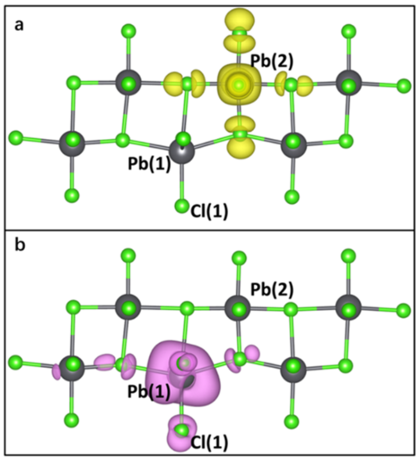

Figure 5. Partial charge density contours of (a) the hole and (b) the electron wave functions of the most stable exciton in $C_4N_2H_{14}PbCl_4$. The charge density on the isodensity surface is 0.0005 e/Bohr^3.

Table 3. Calculated Exciton Trapping Energies and Emission Energies at V_{Cl}^+, V_{Mol}^-, and V_{Pb}^{2-} as Well as the Red Shift of the Emission Energies from the Calculated STE Emission Energy (2.13 eV)[a]

	V_{Cl}^+	V_{Mol}^-	V_{Pb}^{2-}
exciton trapping energy (eV)	0.72	0.17	0.15
emission energy (eV)	1.32	1.88	1.79
red shift from STE emission (eV)	0.81	0.25	0.34

[a] All calculations are PBE0 calculations including the SOC.

STE emission peak by about 0.28 eV) is likely due to the V_{Mol}^-- or V_{Pb}^{2-}-bound excitons. The V_{Cl}-bound exciton emission may be quenched by nonradiative recombination.

Accordingly, this unique inverse excitation-dependent PL can be attributed to the presence of two emitting excited states as confirmed by DFT calculations. In particular, on above-gap photoexcitation, the system is excited to the FE excited states, followed by selective energy transfer/relaxation to defect-related excited states due to their lower energy. On subgap photoexcitation, the system is excited to subgap excited states with energy transfer/relaxation to STE excited states. In this sense, we infer that the defect density is dependent on the excitation energy, similar to the cases in CdF_2 and $Al_xGa_{1-x}As$.[35,36] Specifically, high-energy irradiation can lead to localized reversible bond breaking associated with the formation of more metastable defect excited states, while lower-energy irradiation results in more transient structural distortion to form STE excited states. This could explain the entirely different photophysical properties of the three 1D hybrids that exhibit similar packing modes. As we discussed in the structural part, the level of distortion, $C_4N_2H_{14}SnBr_4$ > $C_4N_2H_{14}PbCl_4$ > $C_4N_2H_{14}PbBr_4$, gives rise to a contrary level of photoinduced bond-breaking difficulty. As a result, on UV irradiation, $C_4N_2H_{14}PbBr_4$ does not show defect-related emission[24] while $C_4N_2H_{14}SnBr_4$ suffers from the photoinduced structural transformation from 1D to 0D[26] owing to bond-breaking upon photoexcitation. Therefore, a straightforward explanation of the excitation-dependent emission is that the population of two emission centers relies heavily on the excitation energy.

In summary, we have developed a new 1D organic lead chloride hybrid with inverse excitation-dependent broadband emission. The emission can be readily tuned by controlling the excitation energy, giving rise to broad emissions ranging from 500 to 570 nm. Experimental and computational studies show that the organic lead chloride hybrid exhibits two emission centers corresponding to defect-related excitons and STEs. Competition between these centers results in the complex excitation-dependent emission. This work not only enriches the family of less explored low-dimensional organic metal halide hybrids but also serves as a research tool for the intriguing excitation-dependent emission in crystalline materials. Moreover, we have observed a distortion−defect correlation which helps to predict the photophysics in those underexplored 1D organic metal halide hybrids for photovoltaic and light emission devices.

DOI: 10.1021/acsenergylett.8b00661
ACS Energy Lett. 2018, 3, 1443−1449

■ ASSOCIATED CONTENT

Supporting Information

The Supporting Information is available free of charge on the ACS Publications website at DOI: 10.1021/acsenergylett.8b00661.

Experimental/computational methods, crystal data, and photoluminescence properties of the fabricated hybrid (PDF)

1D $C_4N_2H_{14}PbCl_4$ (CIF)

■ AUTHOR INFORMATION

Corresponding Authors

*E-mail: agdong@fudan.edu.cn.

*E-mail: bma@fsu.edu.

*E-mail: mhdu@ornl.gov.

ORCID

Shiyou Chen: 0000-0002-4039-8549

Tiglet Besara: 0000-0002-2143-2254

Mao-Hua Du: 0000-0001-8796-167X

Biwu Ma: 0000-0003-1573-8019

Angang Dong: 0000-0002-9677-8778

Author Contributions

⊥G.W. and C.Z. contributed equally.

Notes

The authors declare no competing financial interest.

■ ACKNOWLEDGMENTS

A.D. acknowledges support from MOST (2017YFA0207303, 2014CB845602), Key Basic Research Program of Science and Technology Commission of Shanghai Municipality (17JC1400100), Shanghai International Science and Technology Cooperation Project (15520720100), and NSFC (21733003). C.Z. and B.M. acknowledge the support from the National Science Foundation (DMR-1709116 and CHE-1664661). B.M. also acknowledges support from the Senior Visiting Scholar Foundation of Key Laboratory at Fudan University. The work at ORNL was supported by the U.S. Department of Energy, Office of Science, Basic Energy Sciences, Materials Sciences, and Engineering Division. D.H. and S.C. were supported by NSFC under Grant Nos. 61574059 and 61722402, Shu-Guang program (15SG20), and CC of ECNU. This manuscript has been co-authored by UT-Battelle, LLC under Contract No. DE-AC05-00OR22725 with the U.S. Department of Energy. The United States Government retains and the publisher, by accepting the article for publication, acknowledges that the United States Government retains a non-exclusive, paid-up, irrevocable, world-wide license to publish or reproduce the published form of this manuscript, or allow others to do so, for United States Government purposes. The Department of Energy will provide public access to these results of federally sponsored research in accordance with the DOE Public Access Plan (http://energy.gov/downloads/doe-public-access-plan).

■ REFERENCES

(1) Gan, Z.; Xu, H.; Hao, Y. Mechanism for excitation-dependent photoluminescence from graphene quantum dots and other graphene oxide derivates: consensus. debates and challenges. *Nanoscale* **2016**, *8*, 7794−7807.

(2) Dong, Y.; Pang, H.; Yang, H.; Guo, C.; Shao, J.; Chi, Y.; Li, C.; Yu, T. Carbon-based dots co-doped with nitrogen and sulfur for high quantum yield and excitation-independent emission. *Angew. Chem., Int. Ed.* **2013**, *52*, 7800−7804.

(3) Sharma, A.; Gadly, T.; Gupta, A.; Ballal, A.; Ghosh, S. K.; Kumbhakar, M. Origin of excitation dependent fluorescence in carbon nanodots. *J. Phys. Chem. Lett.* **2016**, *7*, 3695−3702.

(4) Sun, Y.; Zhou, B.; Lin, Y.; Wang, W.; Fernando, K. S.; Pathak, P.; Meziani, M. J.; Harruff, B. A.; Wang, X.; Wang, H.; et al. Quantum-sized carbon dots for bright and colorful photoluminescence. *J. Am. Chem. Soc.* **2006**, *128*, 7756−7757.

(5) Dong, Y.; Shao, J.; Chen, C.; Li, H.; Wang, R.; Chi, Y.; Lin, X.; Chen, G. Blue luminescent graphene quantum dots and graphene oxide prepared by tuning the carbonization degree of citric acid. *Carbon* **2012**, *50*, 4738−4743.

(6) Shen, J.; Zhu, Y.; Chen, C.; Yang, X.; Li, C. Facile preparation and upconversion luminescence of graphene quantum dots. *Chem. Commun.* **2011**, *47*, 2580−2582.

(7) Zhu, S.; Zhang, J.; Liu, X.; Li, B.; Wang, X.; Tang, S.; Meng, Q.; Li, Y.; Shi, C.; Hu, R.; Yang, B. Graphene quantum dots with controllable surface oxidation, tunable fluorescence and up-conversion emission. *RSC Adv.* **2012**, *2*, 2717−2720.

(8) Pan, D.; Zhang, J.; Li, Z.; Wu, M. Hydrothermal route for cutting graphene sheets into blue-luminescent graphene quantum dots. *Adv. Mater.* **2010**, *22*, 734−738.

(9) Cushing, S. K.; Li, M.; Huang, F.; Wu, N. Origin of strong excitation wavelength dependent fluorescence of graphene oxide. *ACS Nano* **2014**, *8*, 1002−1013.

(10) Xu, Q.; Zhou, Q.; Hua, Z.; Xue, Q.; Zhang, C.; Wang, X.; Pan, D.; Xiao, M. Single-particle spectroscopic measurements of fluorescent graphene quantum dots. *ACS Nano* **2013**, *7*, 10654−10661.

(11) Zhu, S.; Zhang, J.; Qiao, C.; Tang, S.; Li, Y.; Yuan, W.; Li, B.; Tian, L.; Liu, F.; Hu, R.; et al. Strongly green-photoluminescent graphene quantum dots for bioimaging applications. *Chem. Commun.* **2011**, *47*, 6858−6860.

(12) Zhu, S.; Zhang, J.; Tang, S.; Qiao, C.; Wang, L.; Wang, H.; Liu, X.; Li, B.; Li, Y.; Yu, W.; et al. Surface chemistry routes to modulate the photoluminescence of graphene quantum dots: From fluorescence mechanism to up-conversion bioimaging applications. *Adv. Funct. Mater.* **2012**, *22*, 4732−4740.

(13) Dong, H.; Tang, S.; Hao, Y.; Yu, H.; Dai, W.; Zhao, G.; Cao, Y.; Lu, H.; Zhang, X.; Ju, H. Fluorescent MoS2 quantum dots: ultrasonic preparation, up-conversion and down-conversion bioimaging, and photodynamic therapy. *ACS Appl. Mater. Interfaces* **2016**, *8*, 3107−3114.

(14) Zhou, C.; Tian, Y.; Yuan, Z.; Lin, H.; Chen, B.; Clark, R.; Dilbeck, T.; Zhou, Y.; Hurley, J.; Neu, J.; et al. Highly efficient broadband yellow phosphor based on zero-dimensional tin mixed-halide perovskite. *ACS Appl. Mater. Interfaces* **2017**, *9*, 44579−44583.

(15) Saparov, B.; Mitzi, D. B. Organic−inorganic perovskites: structural versatility for functional materials design. *Chem. Rev.* **2016**, *116*, 4558−4596.

(16) Saidaminov, M. I.; Mohammed, O. F.; Bakr, O. M. Low-dimensional-networked metal halide perovskites: the next big thing. *ACS Energy Lett.* **2017**, *2*, 889−896.

(17) Lin, H.; Zhou, C.; Tian, Y.; Siegrist, T.; Ma, B. Low-dimensional organometal halide perovskites. *ACS Energy Lett.* **2018**, *3*, 54−62.

(18) Protesescu, L.; Yakunin, S.; Bodnarchuk, M. I.; Krieg, F.; Caputo, R.; Hendon, C. H.; Yang, R.; Walsh, A.; Kovalenko, M. V. Nanocrystals of Cesium lead halide perovskites ($CsPbX_3$, X = Cl, Br, and I): novel optoelectronic materials showing bright emission with wide color gamut. *Nano Lett.* **2015**, *15*, 3692−3696.

(19) Protesescu, L.; Yakunin, S.; Bodnarchuk, M. I.; Bertolotti, F.; Masciocchi, N.; Guagliardi, A.; Kovalenko, M. V. Monodisperse formamidinium lead bromide nanocrystals with bright and stable green photoluminescence. *J. Am. Chem. Soc.* **2016**, *138*, 14202−14205.

(20) Dohner, E. R.; Hoke, E. T.; Karunadasa, H. I. Self-assembly of broadband white-light emitters. *J. Am. Chem. Soc.* **2014**, *136*, 1718−1721.

(21) Dohner, E. R.; Jaffe, A.; Bradshaw, L. R.; Karunadasa, H. I. Intrinsic white-light emission from layered hybrid perovskites. *J. Am. Chem. Soc.* **2014**, *136*, 13154−13157.

(22) Mao, L.; Wu, Y.; Stoumpos, C. C.; Wasielewski, M. R.; Kanatzidis, M. G. White-light emission and structural distortion in new corrugated two-dimensional lead bromide perovskites. *J. Am. Chem. Soc.* **2017**, *139*, 5210−5215.

(23) Trigui, A.; Abid, H.; Mlayah, A.; Abid, Y. Optical properties and vibrational studies of a new self-assembled organic−inorganic nanowire crystal $(C_6H_{13}N_3)\ _2Pb_3I_{10}$. *Synth. Met.* **2012**, *162*, 1731−1736.

(24) Yuan, Z.; Zhou, C.; Tian, Y.; Shu, Y.; Messier, J.; Wang, J. C.; van de Burgt, L. J.; Kountouriotis, K.; Xin, Y.; Holt, E.; et al. One-dimensional organic lead halide perovskites with efficient bluish white-light emission. *Nat. Commun.* **2017**, *8*, 14051.

(25) Zhou, C.; Tian, Y.; Khabou, O.; Worku, M.; Zhou, Y.; Hurley, J.; Lin, H.; Ma, B. Manganese-doped one-dimensional organic lead bromide perovskites with bright white emissions. *ACS Appl. Mater. Interfaces* **2017**, *9*, 40446−40451.

(26) Zhou, C.; Tian, Y.; Wang, M.; Rose, A.; Besara, T.; Doyle, N. K.; Yuan, Z.; Wang, J. C.; Clark, R.; Hu, Y.; Siegrist, T.; Lin, S.; Ma, B. Low-dimensional organic tin bromide perovskites and their photo-induced structural transformation. *Angew. Chem., Int. Ed.* **2017**, *56*, 9018−9022.

(27) Kamminga, M. E.; de Wijs, G. A.; Havenith, R. W. A.; Blake, G. R.; Palstra, T. T.M. The role of connectivity on electronic properties of lead iodide perovskite-derived compounds. *Inorg. Chem.* **2017**, *56*, 8408−8414.

(28) Tathavadekar, M.; Krishnamurthy, S.; Banerjee, A.; Nagane, S.; Gawli, Y.; Suryawanshi, A.; Bhat, S.; Puthusseri, D.; Mohite, A. D.; Ogale, S. Low-dimensional hybrid perovskites as high performance anodes for alkali-ion batteries. *J. Mater. Chem. A* **2017**, *5*, 18634−18642.

(29) Cortecchia, D.; Neutzner, S.; Kandada, A. R. S.; Mosconi, E.; Meggiolaro, D.; Angelis, F. D.; Soci, C.; Petrozza, A. Broadband emission in two-dimensional hybrid perovskites: The role of structural deformation. *J. Am. Chem. Soc.* **2017**, *139*, 39−42.

(30) Zhao, W.; Ghorannevis, Z.; Chu, L.; Toh, M.; Kloc, C.; Tan, P.; Eda, G. Evolution of Electronic Structure in Atomically Thin Sheets of WS_2 and WSe_2. *ACS Nano* **2013**, *7*, 791−797.

(31) Kim, S.; Lee, K.; Kim, S.; Kwon, O. P.; Heo, J. H.; Im, S. H.; Jeong, S.; Lee, D. C.; Kim, S. W. Origin of photoluminescence from colloidal gallium phosphide nanocrystals synthesized via a hot-injection method. *RSC Adv.* **2015**, *5*, 2466−2469.

(32) Zhang, Y.; Yin, J.; Parida, M. R.; Ahmed, G. H.; Pan, J.; Bakr, O. M.; Bredas, J. L.; Mohammed, O. F. Direct-indirect nature of the bandgap in lead-free perovskite nanocrystals. *J. Phys. Chem. Lett.* **2017**, *8*, 3173−3177.

(33) Tauc, J.; Grigorovici, R.; Vancu, A. Optical properties and electronic structure of amorphous germanium. *Phys. Status Solidi B* **1966**, *15*, 627−637.

(34) Tongay, S.; Suh, J.; Ataca, C.; Fan, W.; Luce, A.; Kang, J. S.; Liu, J.; Ko, C.; Raghunathanan, R.; Zhou, J.; Ogletree, F.; Li, J.; Grossman, J. C.; Wu, J. Defects activated photoluminescence in two-dimensional semiconductors: interplay between bound, charged, and free excitons. *Sci. Rep.* **2013**, *3*, 2657.

(35) Biegelsen, D. K.; Street, R. A. Photoinduced defects in chalcogenide glasses. *Phys. Rev. Lett.* **1980**, *44*, 803−806.

(36) Nissilä, J.; Saarinen, K.; Hautojärvi, P.; Suchocki, A.; Langer, J. M. Universality of the bond-breaking mechanism in defect bistability: observation of open volume in the deep states of In and Ga in CdF2. *Phys. Rev. Lett.* **1999**, *82*, 3276−3279.